ACS Photonics

Article

Cite This: ACS Photonics 2018, 5, 1115−1122

Highly Broadband Absorber Using Plasmonic Titanium Carbide (MXene)

Krishnakali Chaudhuri,[†] Mohamed Alhabeb,[‡] Zhuoxian Wang,[†] Vladimir M. Shalaev,[†] Yury Gogotsi,[‡] and Alexandra Boltasseva*[,†]

[†]Birck Nanotechnology Center, School of Electrical and Computer Engineering, Purdue University, West Lafayette, Indiana 47907, United States

[‡]A. J. Drexel Nanomaterials Institute and Department of Materials Science and Engineering, Drexel University, Philadelphia, Pennsylvania 19104, United States

Supporting Information

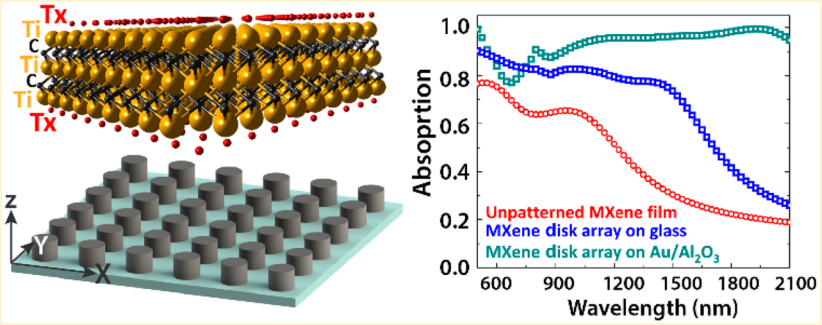

ABSTRACT: Control of light transmission and reflection through nanostructured materials has led to demonstration of metamaterial absorbers that have augmented the performance of energy harvesting applications of several optoelectronic and nanophotonic systems. Here, for the first time, a broadband plasmonic metamaterial absorber is fabricated using two-dimensional titanium carbide ($Ti_3C_2T_x$) MXene. Arrays of nanodisks made of $Ti_3C_2T_x$ exhibit strong localized surface plasmon resonances at near-infrared frequencies. By exploiting the scattering enhancement at the resonances and the optical losses inherent to $Ti_3C_2T_x$ MXene, high-efficiency absorption (~90%) for a wide wavelength window of incident illumination (~1.55 μm) has been achieved.

KEYWORDS: *plasmonics, MXene, absorber, metamaterial*

Versatile capability of light manipulation using plasmonic resonators has led to the development of nanoscale perfect lenses,[1] sensors,[2] absorbers,[3] detectors,[4] light sources,[5,6] and other planar nanophotonic devices. Metamaterial absorbers, in particular, have been shown to bring about some of a new generation of energy harvesting systems such as nanoscale heat sources,[7] photothermal,[8] solar photovoltaic,[9] thermoelectric devices,[10] and photocatalysis.[11] Localized heating through light absorption of metamaterials has led to the demonstration of thermophoresis-assisted and other heat-assisted nanoscale particle manipulation and printing schemes that are now of wide interest for various applications.[12]

Generally, well-known noble metals such as Au[13] and Ag,[14] as well as other lossy metals such as Cu[15] and Ti[16] have been extensively used as plasmonic absorbers. More recently, absorbers with refractory plasmonic compounds (e.g., TiN[3,17]) have been also used in designing devices requiring elevated temperature operation. Furthermore, due to their unique electronic and optical properties, 2D materials such as graphene, transition metal dichalcogenides, and phosphorene have also been implemented in devices with tunable,[18] perfect,[19] and saturable absorption.[20−23] To design plasmonic absorbers, localized surface plasmon resonances in metallic nanoantenna structures are often employed to significantly increase the optical cross-section, which leads to absorption amplification in the spectral range of interest.[24,25] In many of these examples, the operation bandwidth is largely determined by the full width at half-maximum (fwhm) of the plasmonic resonances at play. Therefore, spectrally shifted resonances (from one or more resonating elements) can be harnessed to achieve a large absorption bandwidth.[26,27] However, the collective response of the device is affected by individual antenna geometry besides the interaction of resonances from the neighboring elements. These factors necessitate an absorber device that can combine high-efficiency, robust broadband operation in an ultrathin, easy-to-fabricate, and scalable design.

Recently, 2D transition metal carbides and nitrides called MXenes have drawn a great interest due to their tunable properties and wide range of applications.[28] The chemical

Received: November 28, 2017
Published: January 10, 2018

DOI: 10.1021/acsphotonics.7b01439
ACS Photonics 2018, 5, 1115−1122

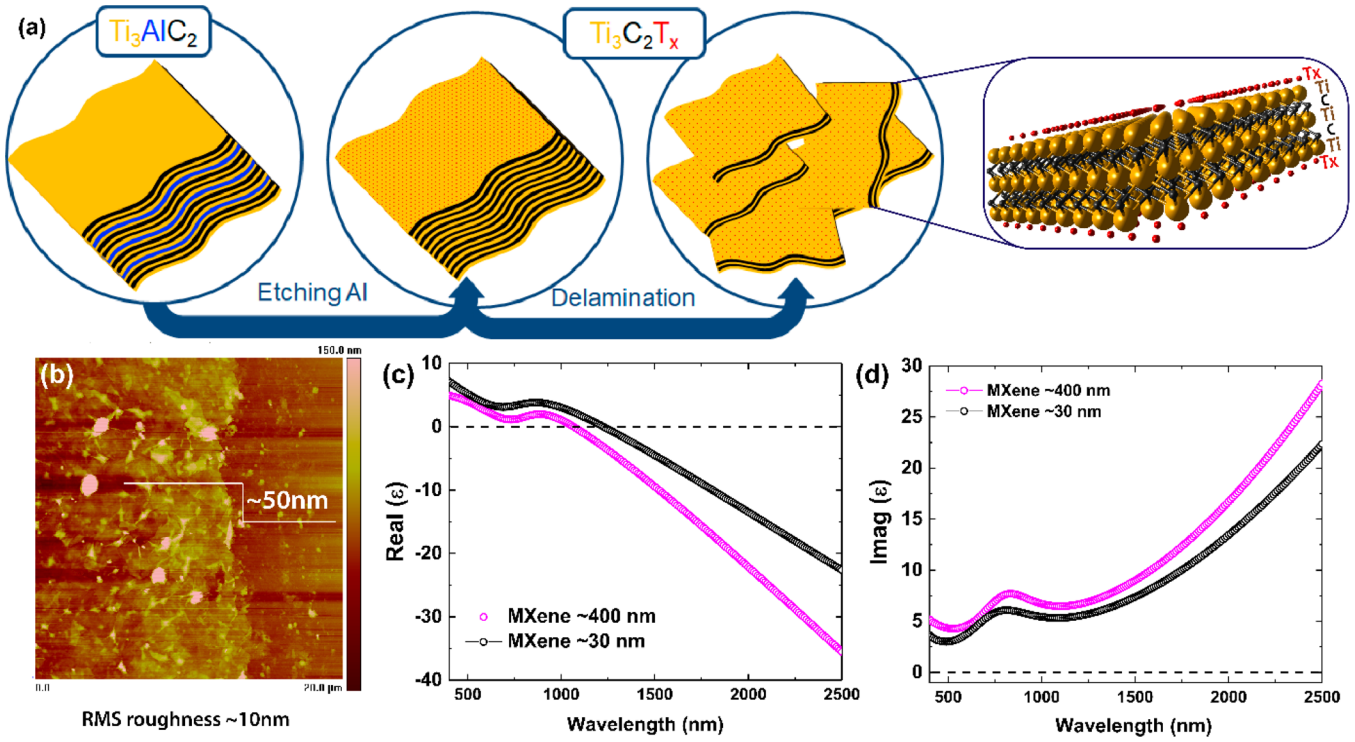

Figure 1. (a) Schematic of synthesis of MXene and the structure of a single layer of $Ti_3C_2T_x$. (b) AFM image of a spin-coated MXene film with a scratch to measure the thickness (indicated inside). (c, d) Experimentally measured real (c) and imaginary (d) parts of permittivity (ε) of $Ti_3C_2T_x$ films with a thickness of 30 and 400 nm.

formula of MXene compositions is written as $M_nX_{n+1}T_x$, where M denotes the transition metal (e.g., Ti, Ta, Nb, Zr, Hf, Cr, Mo, etc.), X is either C and/or N, and T represents surface functional groups.[29,30] In contrast to other 2D materials often produced by mechanical exfoliation of their bulk counterparts, single to few-layer flakes of MXene are isolated through chemical exfoliation of bulk ternary carbides and nitrides, known as "MAX" phase, in fluorine-containing solutions.[31] More than 60 varieties of MXenes have been predicted, and more than 20 have been experimentally synthesized, making them among the fastest growing and the most diverse 2D materials.[30] In particular, titanium carbide ($Ti_3C_2T_x$) MXene exhibits high electrical conductivity[32] and has been explored in a variety of applications such as transparent electrodes,[33] metal ion batteries,[34] supercapacitors,[35−37] and electromagnetic interference shielding.[38] Utilizing the optical properties of ($Ti_3C_2T_x$) MXene, other applications such as effective light to heat conversion,[39] saturable absorption for mode-locked lasing,[40] and surface-enhanced Raman scattering (SERS) substrate[41,42] have also been demonstrated. However, investigations of ($Ti_3C_2T_x$) MXenes in the context of nanophotonics and plasmonics[25,43] have been limited in both theory[44] and experiment.[41,45]

In this work, for the first time, plasmonic resonances in nanostructured $Ti_3C_2T_x$ MXene have been used to create a simple and easy-to-fabricate metasurface[46] device. Large absorption over a broad bandwidth (~1.55 μm), covering a significant visible to near-IR spectral window, was obtained by utilizing both the large optical absorption and the scattering enhancement of plasmonic resonances of nanostructured $Ti_3C_2T_x$ at longer wavelengths. Integrating MXenes with planar metamaterials is expected to have a significant impact on the large-scale energy harvesting systems by improving the conversion efficiency of light to heat, light to electricity, heat to electricity generation, etc.

Theory and Implementation Discussion. $Ti_3C_2T_x$ is the first discovered and the most studied MXene; however, it was chosen as the primary focus for this work due to its high metallic conductivity,[31,47] environmental and chemical stability,[47] controllable surface hydrophilicity,[48] dynamic control through easy intercalation,[49] and scalable synthesis (~100 g per batch in the lab). Due to the wet chemical synthesis in fluorine-containing media, the surface of 2D $Ti_3C_2T_x$ sheets is terminated with functional groups (T_x) such as −F,−O, and −OH.[50] Although the surface chemistry can affect some properties such as the hydrophilicity, electrical conductivity, and free carrier concentration,[50,51] the core layer of Ti metal in $Ti_3C_2T_x$ is predominantly behind the high electrical conductivity of this MXene. Moreover, it has been shown that the surface of $Ti_3C_2T_x$ can be modified as per requirements of specific application.[52,53] In our experiments, the $Ti_3C_2T_x$ was prepared via the minimally intensive layer delamination (MILD) method (Figure 1(a)), which results in flakes of $Ti_3C_2T_x$ MXene with 1−10 μm in the lateral dimension,[47] and we recently described it in detail elsewhere.[32] With larger single- or few-layer flakes in the initial solution dispersion, spin-coated thin films become uniform over a larger area, which is critical for subsequent processing steps (for details, see Methods).

The colloidal solution of single- to few-layer flakes of MXene can be used for vacuum-assisted filtration[54] or spray coating[38] to create large-area freestanding micrometer-thick sheets of MXene, as well as produce nanometer-thin films by spin coating on a substrate of choice[55] (Figure S2), rendering the process highly scalable and cost-effective. In this work, thin MXene films of varying thicknesses (~30−400 nm) were used.

DOI: 10.1021/acsphotonics.7b01439
ACS Photonics 2018, 5, 1115−1122

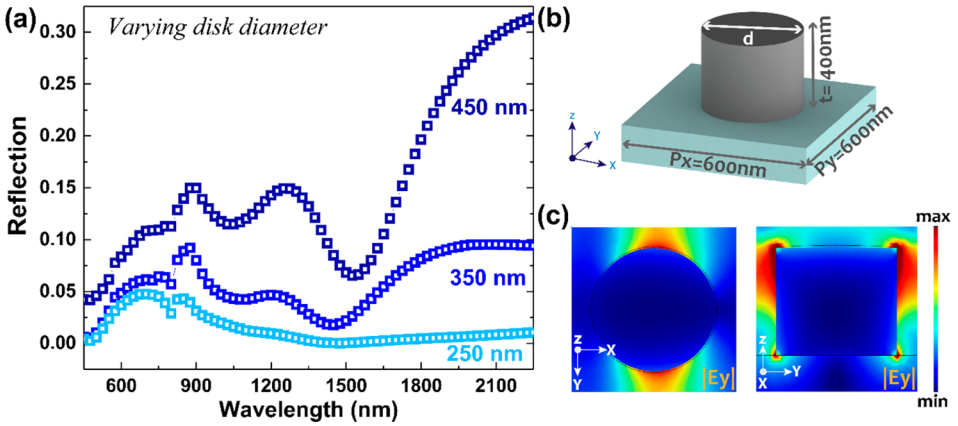

Figure 2. (a) FEM simulation generated reflection spectra for $Ti_3C_2T_x$ disk arrays on a glass substrate with varying disk diameters (450, 350, and 250 nm, respectively) for TE-polarized incident light, (b) schematic of a typical unit cell with critical dimensions indicated, and (c) electric field intensity map at a horizontal (at $z = t/2$ from the top of the disk, left image) and vertical ($x = d/2$ from the edge of disk, right image) planar cross-section through the disk. Localized surface plasmon induced dipolar resonant mode at a wavelength (λ) of ~1.26 μm can be inferred.

A bulk in-plane conductivity of ~6500 ± 800 S/cm in a N_2 atmosphere and ~2000 S/cm in open air, a carrier density of ~$(3.1 \pm 0.7) \times 10^{22}$ cm^{-3}, and Hall carrier mobility of ~0.9 ± 0.1 cm^2 V^{-1} s^{-1} have been reported previously for $Ti_3C_2T_x$ films of similar thickness.[56] Continuous films with thickness down to ~5 nm, exhibiting similar metallic characteristics, have also been successfully demonstrated.[56] A high conductivity of ~4600 ± 1100 S/cm (in air) and a field effect mobility of ~2.6 ± 0.7 cm^2 V^{-1} s^{-1} have been reported for individual $Ti_3C_2T_x$ flakes.[47] The low carrier mobility in these films has been explained intuitively by inter-flake hopping-type conduction.[56,57] Thicknesses of the films were measured using a profilometer and/or atomic force microscope (AFM) after carefully making a scratch on the film (Figure 1(b)).

First, the spectral dependence of real and imaginary parts of dielectric permittivity (ϵ) was measured for the spin-coated $Ti_3C_2T_x$ films of varying thickness, using a variable-angle spectroscopic ellipsometry (VASE) setup (Figure S1). One Drude term and two Lorentz-type oscillators are used to fit the measured raw VASE data and extract the parameters of the dielectric functions (Table S1). The Drude term describes the metal-like behavior, whereas the two Lorentz oscillators account for the interband electron transitions. A dielectric to metallic crossover at ~1.07 μm corroborates the existence of surface plasmon polaritons (SPPs) at the MXene interface in the near- and mid-infrared (IR) frequencies. Figure 1(c, d) compare the dielectric permittivity values measured from MXene films of thickness ~30 and ~400 nm. A large imaginary part of the relative dielectric permittivity (Im(ϵ)) was observed for both films, increasing with the thickness (higher for a thickness of about 400 nm). In addition, thicker films appear to be more metallic (shorter crossover wavelength for a thickness of about 400 nm). Optical losses were attributed in part to the intrinsic absorption due to interband transitions (at ~5.36 eV (0.23 μm)) and ~1.54 eV (0.8 μm))[58] and to losses stemming from surface roughness- and bulk disorder-related scattering of carriers (Figure 1(d)). Lorentz oscillators at similar frequencies obtained through ellipsometry measurement are summarized in Table S1.

Second, we evaluated the performance of $Ti_3C_2T_x$ nanostructures through numerical simulations by utilizing the optical properties retrieved from ellipsometric characterization of the continuous MXene films. Full wave three-dimensional (3D) finite-element method (FEM) simulations were performed using the commercially available multiphysics tool "COMSOL" for large-area arrays of disks/pillars of MXene on glass substrates with varying diameters and thicknesses. The measured frequency-dispersive dielectric permittivity values of the MXene film were input into the model. The optical parameters (transmission, T, and reflection, R) as a function of the wavelength were calculated under excitation of TM/TE-polarized light. An incident angle of 20° was assumed for this study (for details on the experimental setup, see Supporting Information Section 1), unless specified otherwise. The calculated reflection spectra from arrays of disks/pillars with varying diameter (d) as 250, 350, and 450 nm are shown in Figure 2(a). Corresponding transmission and absorption spectra are shown in Figure S3. A periodic spacing (P) of 600 nm and thickness (t) of 400 nm were used for these calculations. The plot clearly indicates signatures of a resonance (peak in the resonance spectra) at ~1.26 μm and for d = 450 nm. This is determined to be a localized surface plasmon (LSP) resonance from the cross-section electric field maps shown in Figure 2(c) and displacement current maps (shown in Figure S4-i). As expected, optical losses cause the resonance to be broad and, with reduced resonator dimension, the resonance peak frequency blue shifts. But, with relatively less metallic real part of the relative dielectric permittivity Re(ϵ) along with the large enough Im(ϵ) at the blue-shifted wavelength, the quality factor of the resonance drops significantly (the peak almost disappears for disk d = 250 nm). Additionally, for smaller d, a lower filling fraction (disk area/unit cell area) allows increased transmission (T) through the structure. MXene resonators have dielectric like optical properties at higher energies and, when surrounded by a lower index medium (air), create a weak lattice mode in the periodic array (small peak in the reflection spectra at ~0.9 μm). For λ < 1 μm, the MXene disks support weak photonic resonance modes that also contribute in part to small enhancement of absorption in the visible spectral window (Figure S4-ii). Deeper into the near-IR, beyond ~1.8 μm, MXene is more Drude-type metallic, which renders large reflection amplitude.

Losses inherent to the bulk MXene and existence of LSP resonances in nanostructures led us to investigate the potential of nanopatterned MXene as an absorber metamaterial. In the simulation, the absorption ($A = 1 - T - R$) is calculated as a

DOI: 10.1021/acsphotonics.7b01439
ACS Photonics 2018, 5, 1115−1122

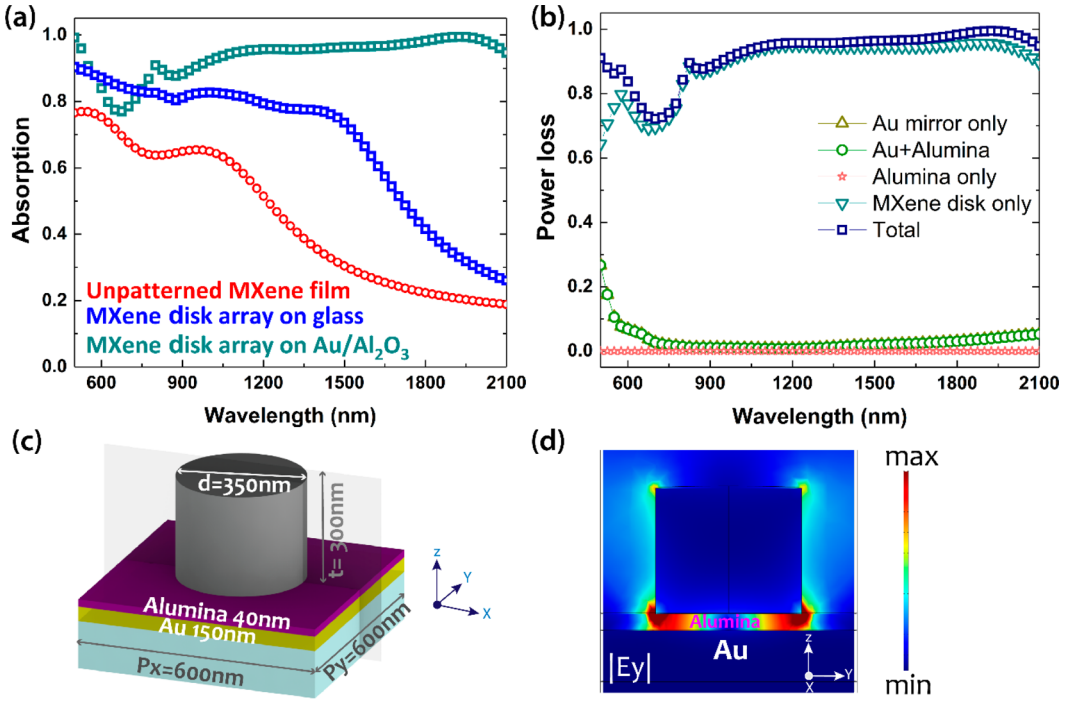

Figure 3. (a) Simulated absorption spectra comparison of unpatterned MXene film, MXene disk array on glass, and MXene disk array on Au/alumina (incident light is TE polarized, angle of incidence is 20°). (b) Comparison of volume integrated power loss density (simulated) in the individual components, e.g., MXene disk only, Au mirror only, alumina only, Au+alumina, and total structure. (c) Schematic of a unit cell with relevant dimensions and (d) vertical cross-section ($x = d/2$ from edge of disk) electric field map at $\lambda \approx 1.85$ μm.

function of the incident excitation wavelength (λ). Dimensions of different components were optimized to maximize the amplitude as well as the absorption bandwidth. For an array of $Ti_3C_2T_x$ disks with d = 450 nm, P = 600 nm, and t = 400 nm sitting on a glass substrate, ~85% absorption efficiency was achieved across a 0.4−1.4 μm bandwidth (blue curve in Figure 3(a)) Simulations were also performed to calculate the absorption from an as-coated continuous film of the same thickness (red curve in Figure 3(a)). Absorption in the visible and very near-IR originates largely from inter- and intraband transitions of electrons.[44,58] At longer wavelengths, resonance aids increased scattering cross-section. Together, these two phenomena create high absorption efficiency over a large spectral window. However, the absorption in the patterned disk array shows significant improvement (~2.5 times at ~1.5 μm) when compared to the unpatterned film (Figure 3(a)).

To further increase the performance of this broadband absorber design, we added a thin mirror (Au) and dielectric spacer layer (Al_2O_3) underneath the disk array. Schematic of a unit cell is shown in Figure 3(c). This geometrical configuration supports gap surface plasmon (GSP) resonance.[59] This mode is formed when a resonator is placed close to metal surface but separated by a nanoscale gap (in a practical scenario, a dielectric spacer layer).[60] The mode is the result of interaction of surface plasmons on the two adjacent dielectric−metal interfaces and efficient reflection from the ends of the finite dimension resonator on the top surface. The forward and backward propagating GSPs interfere constructively and destructively to create standing wave resonances in a Fabry−Perot-like cavity at certain frequencies. This causes a high electric field confinement in the gap region, which can largely enhance the power efficiency of the device.[61] Figure 3(d) shows the cross-section electric field map of this gap plasmon resonance. The mode (at $\lambda \approx 1.85$ μm in this structure) displays a strong field confinement in the alumina (Al_2O_3) spacer layer. The Au layer at the bottom of the structure is optically thick and blocks all light transmission. Optical properties of Au and alumina used in the simulation were measured by the VASE technique (summarized in Figure S6). This mode attribute can be controlled by the optical properties and thickness of the spacer dielectric, as well as the properties of the top resonator. This extended parameter space was utilized for obtaining maximum absorption (>90%) over an even broader operating bandwidth. Through optimization in full wave 3D FEM simulations, design parameters were determined to be a 40 nm thick alumina spacer on top of a 150 nm thick Au film and the periodic MXene disk array to be of d = 350 nm, t = 300 nm, and P = 600 nm.

Absorption in this gap plasmon structure mainly originates from the MXene disk for almost the entire bandwidth of investigation. Absorption contributions for different structural components (MXene disk only, Au mirror only, Al_2O_3 spacer only, Au + Al_2O_3, and all together) were calculated separately by volumetric integration of power loss density ($P_{loss} = \frac{1}{2}\omega\, Im(\varepsilon)|E|^2$), and the comparison is shown in Figure 3(b). Localized resonances, as seen in the electric field intensity maps, aid field concentration near the surfaces of the MXene resonators, which is the main source of losses in near-IR. The low quality factor of this hybrid resonance mode at ~1.85 μm is responsible for achieving near-perfect absorption over a broad region of the spectrum. The noble metal (Au) back mirror is highly metallic at longer wavelengths (large negative Re(ε)) and therefore functions as an almost perfect reflector having negligible contribution to total absorption. Between 600 and 900 nm MXene behaves as a lossy dielectric. The small dip in the absorption spectra at ~680 nm stems from a hybrid resonant mode. This arises from weak coupling between a

DOI: 10.1021/acsphotonics.7b01439
ACS Photonics 2018, 5, 1115−1122

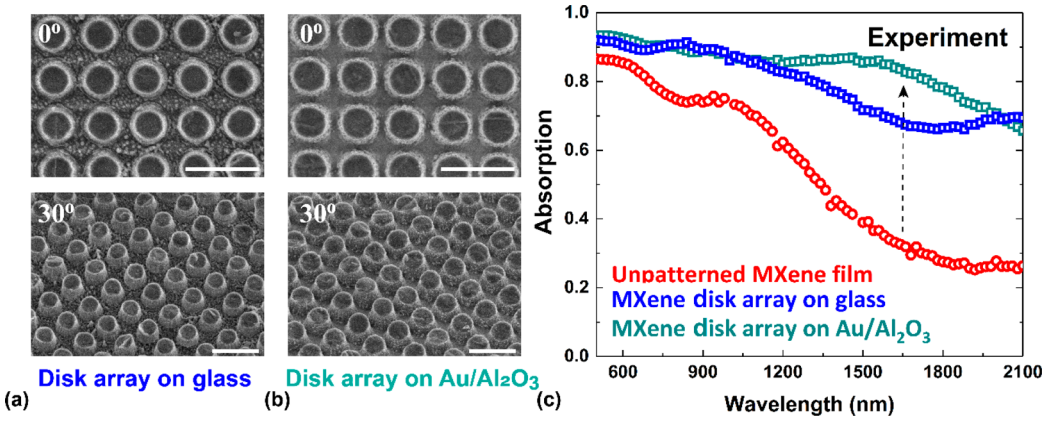

Figure 4. SEM images collected from 0° (top) and 30° inclined angles (bottom) from the fabricated (a) disk array on glass, (b) disk array on Au/alumina (scale bars indicate 1 μm in all images), and (c) measured absorption spectra comparison for the two types of disk arrays and unpatterned MXene film (incident light is TE polarized; angle of incidence is 20°).

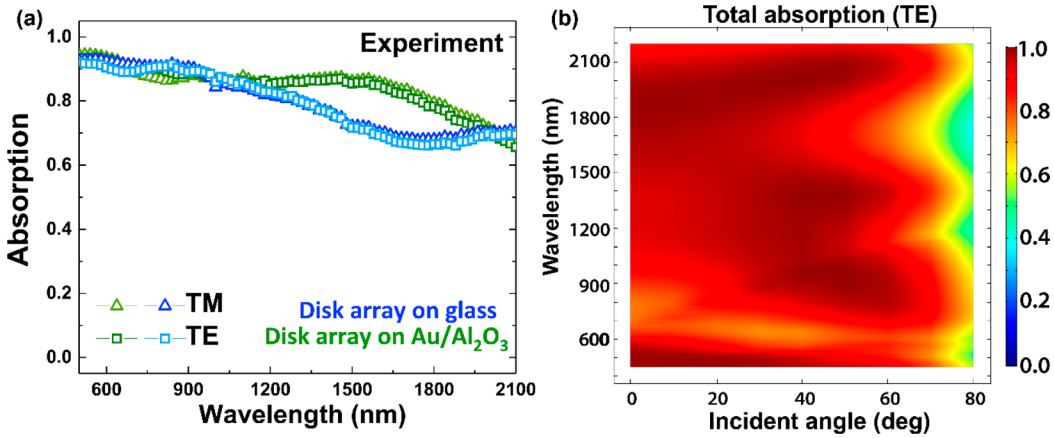

Figure 5. (a) Experimentally measured absorption spectra for two orthogonal polarizations (TE and TM) for both fabricated disk array designs (on glass and on the Au/alumina back layer) at a 20° angle of incidence. (b) Simulated angular bandwidth for the disk array on Au/alumina for TE polarized incidence. The map plots wavelength (λ) vs incident excitation angle (measured from normal), and the amplitude of absorption is indicated by the color bar.

photonic mode in the MXene disk and an SPP-like mode at the Au−alumina interface (Figure S5(b)).[62]

Next, the MXene nanodisk arrays were fabricated following the two designs discussed above (Figure 4(a, b)), and optical scattering parameters were measured using a VASE setup (see Methods for details of fabrication and measurement). Reflection (R) and transmission (T) were measured for different incident angles and both orthogonal polarizations (TM and TE). Absorption (A) is calculated as $A = 1 - T - R$, as before and is shown in Figure 4(c). Large absorption (≥80%) over 0.4 to 1.3 μm is observed for just the disk array on glass (blue curve in Figure 4(c)). For the other design, with the disk array sitting on an Au/Al_2O_3 bilayer stack, similar large absorption (~85−90%) is obtained, but in addition, the bandwidth is stretched further to ~1.55 μm (green curve in Figure 4(c)). Significant enhancement of absorption as compared to the unpatterned MXene film throughout the entire bandwidth of operation was demonstrated in the experiments. A good qualitative agreement in comparative trend between the experimentally measured curves (~2 times improvement in absorption in the MXene disk array on Au/alumina over an unpatterned film of similar thickness (t) at $\lambda \approx 1.6$ μm) with the ones obtained through simulation is apparent.

The measured absorption spectra for both TE and TM polarized excitation match almost perfectly for low incident angles (<~40°), as shown in Figure 5(a). An incident angle dependence of the absorption spectra was observed for both orthogonal polarizations. This was extracted in simulation and summarized in Figure 5(b) and Figure S7. Large absorption over the entire bandwidth of interest was maintained with incident angles ranging from 0° to 65° for TE polarized incident light (all angles were calculated from normal, i.e., 0° is equivalent to normal incidence). However, for TM polarized incidence, this angular bandwidth ranged from 0° to 45° (Figure S7).

Deviation of the observed experimental data from the simulated ones stems from a few factors. It is well known that surface plasmon-polaritons and the nature of LSP and GSP resonances have high sensitivity to the adjacent environment and geometry of the resonators.[25] This has propelled prolific use of plasmonic resonators in sensing.[63,64] Similarly, in the absorber design discussed here, the geometry as well as the surface chemistry of $Ti_3C_2T_x$ MXene affects the LSP and GSP resonances and in turn the overall absorption spectrum.

DOI: 10.1021/acsphotonics.7b01439
ACS Photonics 2018, 5, 1115−1122

CONCLUSION

In this work, we used nanoscale structures of 2D $Ti_3C_2T_x$ MXene to demonstrate localized surface plasmon type resonances. The optical properties of thin films of overlapping flakes of $Ti_3C_2T_x$ are studied and used to design metasurfaces exhibiting broadband absorption. Both proposed MXene-based designs are relatively simple to fabricate into subwavelength-sized disk structures, in contrast to previous reports of plasmonic absorbers with complex geometries. Large operation bandwidth (maximum of ~1.55 μm) and high efficiency (80–90%) are attained. The highly broadband absorber reported here for $Ti_3C_2T_x$, along with the ability to tune the surface properties of MXene, will open doors to investigating MXenes in important applications, such as harvesting energy from light, biomedical imaging, and sensing. With more than 20 MXenes already reported and dozens more predicted, the processing and nanofabrication techniques developed for $Ti_3C_2T_x$ are of high relevance for other members of the MXenes family. This work serves as a first step toward successful integration of MXenes into the field of nanophotonics.

METHODS

$Ti_3C_2T_x$ MXene Thin Film Preparation. Fused silica glass substrates (from PG&O) with dimensions 1.5 cm × 1.5 cm were cleaned with 10 mL of liquid bleach (Sr5900-1 GAL, Fisher Scientific) and diluted in 10 mL of deionized water (DI H_2O) using bath sonication (model 2510R-DTH, Bransonic) for 5 min. The substrates were further bath-sonicated in 20 mL of DI H_2O (4 times for 2 min) and 20 mL of ethanol (4 times for 2 min) before being purged with argon. Prior to spin coating, the glass substrates were further treated with ozone (O_3) plasma for 20 min followed by purging in N_2 to enhance their surface hydrophilicity and to improve the adhesion and the uniformity of the $Ti_3C_2T_x$ coated film.

Spin coating was done by drop casting 200 μL of $Ti_3C_2T_x$ MXene solution (30 mg/mL) on the substrate followed by spinning at 800, 1000, 2000, and 5000 rpm for 1, 1, 4, and 4 min, respectively. $Ti_3C_2T_x$ films coated on the glass substrates were dried during the spinning, while MXene coated on Al_2O_3 substrates was dried in air for 15 min. Both substrates were further dried in a vacuum oven at 150 °C for 15 h. Different thicknesses of coated films were achieved by variation of spinning conditions and the concentration of flakes in the initial solution. For the hybrid design, 10 nm Ti, 150 nm Au, and 40 nm Al_2O_3 were deposited *in situ* by e-beam evaporation technique onto a clean glass substrate by electron beam evaporation. MXene was coated onto this sample using the same method as discussed above.

Simulation. In the commercially available multiphysics tool COMSOL, a wave-optics module has been used to perform full wave finite element method simulations (frequency domain). Direct stationary "PARDISO" solver is chosen for the calculations. Periodic boundary condition and port excitation mode is used. Transmission, reflection, and absorption are calculated using S-parameters. Relevant geometry parameters are discussed in the text above. Experimentally measured spectral dependence of complex dielectric permittivity values for MXene, Au, and alumina (as presented in Figure 1(c, d) and Figure S6(a, b)) were input into the COMSOL model as well.

Fabrication. Electron beam lithography followed by dry etching was used to fabricate the nanostructures. The samples with spin-coated MXene films were dipped into acetone and dried in nitrogen. First, a sacrificial layer of poly(methyl acrylate) (PMMA) (950 A2) was coated followed by baking at 160 °C for 5 min. This layer helps protect the MXene from subsequent lithography processing. After cooling to ambient temperature, a second layer of electron beam resist "Flowable oxide" (FOX-16 by Dow Corning Chemicals) was coated and cured at 120 °C for 3 min. The thickness of this resist layer was ~600 nm. After electron beam exposure, the resist was developed using tetramethylammonium hydroxide (TMAOH) (25% in Ha second layer of electron beam $_2O$) solution for 1 min followed by a 30 s rinse in DI water. Since the MXene surface is hydrophilic and both water and TMAOH are intercalants for MXene, it is crucial to protect the film structure with the PMMA sacrificial layer. At this stage, the intended pattern was transferred onto the resist layer.

In the first step of dry etching, the sacrificial PMMA layer was etched using O_2 plasma. Following that, an inductively coupled plasma of halogenated (BCl_3, Cl_2) and argon (Ar) gas mixtures was used to produce the MXene pillars. To maintain a high degree of anisotropy in the structure, a relatively large source power (850 W), low pressure (0.8 Pa), and a small bias power (60 W) were used. Etching time varied depending on the film thickness. SEM images of the final structure tilted at 30° inclination are shown in Figure 4(a, b).

Optical Measurements. Transmission (T) and reflection (R) were measured for each sample using a VASE setup for two orthogonal polarizations of the incident beam (Supporting Information Section 1). Incident angle was varied from 20° to 80° at steps of 10°. Absorption spectra were then calculated using $A = 1 - T - R$.

ASSOCIATED CONTENT

Supporting Information

The Supporting Information is available free of charge on the ACS Publications website at DOI: 10.1021/acsphotonics.7b01439.

Additional information (PDF)

AUTHOR INFORMATION

Corresponding Author

*E-mail: aeb@purdue.edu.

ORCID

Mohamed Alhabeb: 0000-0002-9460-8548
Zhuoxian Wang: 0000-0002-1299-7384
Yury Gogotsi: 0000-0001-9423-4032
Alexandra Boltasseva: 0000-0002-5988-7625

Notes

The authors declare no competing financial interest.

ACKNOWLEDGMENTS

The authors would like to acknowledge valuable discussions with colleagues Aveek Dutta (Purdue) and Kathleen Maleski (Drexel) during this work. We acknowledge partial funding support for this work by AFOSR MURI Grant FA9550-12-1-0389 and GSU MURI Grant N0001413-1-0649. M. Alhabeb is supported by the Libyan North America Scholarship Program funded by the Libyan Ministry of Higher Education and Scientific Research.

DOI: 10.1021/acsphotonics.7b01439
ACS Photonics 2018, 5, 1115–1122

REFERENCES

(1) Verslegers, L.; Catrysse, P. B.; Yu, Z.; White, J. S.; Barnard, E. S.; Brongersma, M. L.; Fan, S. Planar Lenses Based on Nanoscale Slit Arrays in a Metallic Film. *Nano Lett.* **2009**, *9* (1), 235−238.

(2) Willets, K. A.; Van Duyne, R. P. Localized Surface Plasmon Resonance Spectroscopy and Sensing. *Annu. Rev. Phys. Chem.* **2007**, *58* (1), 267−297.

(3) Li, W.; Guler, U.; Kinsey, N.; Naik, G. V.; Boltasseva, A.; Guan, J.; Shalaev, V. M.; Kildishev, A. V. Refractory Plasmonics with Titanium Nitride: Broadband Metamaterial Absorber. *Adv. Mater.* **2014**, *26* (47), 7959−7965.

(4) Berini, P. Surface Plasmon Photodetectors and Their Applications. *Laser Photonics Rev.* **2014**, *8* (2), 197−220.

(5) Zheludev, N. I.; Prosvirnin, S. L.; Papasimakis, N.; Fedotov, V. A. Lasing Spaser. *Nat. Photonics* **2008**, *2* (6), 351−354.

(6) Meng, X.; Liu, J.; Kildishev, A. V.; Shalaev, V. M. Highly Directional Spaser Array for the Red Wavelength Region. *Laser Photonics Rev.* **2014**, *8* (6), 896−903.

(7) Baffou, G.; Quidant, R. Thermo-Plasmonics: Using Metallic Nanostructures as Nano-Sources of Heat. *Laser Photonics Rev.* **2013**, *7* (2), 171−187.

(8) Coppens, Z. J.; Li, W.; Walker, D. G.; Valentine, J. G. Probing and Controlling Photothermal Heat Generation in Plasmonic Nanostructures. *Nano Lett.* **2013**, *13* (3), 1023−1028.

(9) Mubeen, S.; Lee, J.; Lee, W.; Singh, N.; Stucky, G. D.; Moskovits, M. On the Plasmonic Photovoltaic. *ACS Nano* **2014**, *8* (6), 6066−6073.

(10) Pan, Y.; Tagliabue, G.; Eghlidi, H.; Höller, C.; Dröscher, S.; Hong, G.; Poulikakos, D. A Rapid Response Thin-Film Plasmonic-Thermoelectric Light Detector. *Sci. Rep.* **2016**, *6* (1), 37564.

(11) Naldoni, A.; Riboni, F.; Guler, U.; Boltasseva, A.; Shalaev, V. M.; Kildishev, A. V. Solar-Powered Plasmon-Enhanced Heterogeneous Catalysis. *Nanophotonics* **2016**, *5* (1), 112.

(12) Ndukaife, J. C.; Kildishev, A. V.; Nnanna, A. G. A.; Shalaev, V. M.; Wereley, S. T.; Boltasseva, A. Long-Range and Rapid Transport of Individual Nano-Objects by a Hybrid Electrothermoplasmonic Nanotweezer. *Nat. Nanotechnol.* **2016**, *11* (1), 53−59.

(13) Watts, C. M.; Liu, X.; Padilla, W. J. Metamaterial Electromagnetic Wave Absorbers. *Adv. Mater.* **2012**, *24* (23), 98−120.

(14) Cheng, C.-W.; Abbas, M. N.; Chiu, C.-W.; Lai, K.-T.; Shih, M.-H.; Chang, Y.-C. Wide-Angle Polarization Independent Infrared Broadband Absorbers Based on Metallic Multi-Sized Disk Arrays. *Opt. Express* **2012**, *20* (9), 10376−10381.

(15) Hao, J.; Wang, J.; Liu, X.; Padilla, W. J.; Zhou, L.; Qiu, M. High Performance Optical Absorber Based on a Plasmonic Metamaterial. *Appl. Phys. Lett.* **2010**, *96* (25), 251104.

(16) Ding, F.; Dai, J.; Chen, Y.; Zhu, J.; Jin, Y.; Bozhevolnyi, S. I. Broadband near-Infrared Metamaterial Absorbers Utilizing Highly Lossy Metals. *Sci. Rep.* **2016**, *6* (1), 39445.

(17) Chirumamilla, M.; Chirumamilla, A.; Yang, Y.; Roberts, A. S.; Kristensen, P. K.; Chaudhuri, K.; Boltasseva, A.; Sutherland, D. S.; Bozhevolnyi, S. I.; Pedersen, K. Large-Area Ultrabroadband Absorber for Solar Thermophotovoltaics Based on 3D Titanium Nitride Nanopillars. *Adv. Opt. Mater.* **2017**, *5*, 1700552.

(18) Li, H.; Wang, L.; Zhai, X. Tunable Graphene-Based Mid-Infrared Plasmonic Wide-Angle Narrowband Perfect Absorber. *Sci. Rep.* **2016**, *6* (1), 36651.

(19) Long, Y.; Shen, L.; Xu, H.; Deng, H.; Li, Y. Achieving Ultranarrow Graphene Perfect Absorbers by Exciting Guided-Mode Resonance of One-Dimensional Photonic Crystals. *Sci. Rep.* **2016**, *6* (1), 32312.

(20) Wang, Y.; Li, L.; Wnag, X. Ultrafast Pulse Generation with Black Phosphorus Solution Saturable Absorber. *Laser Phys.* **2017**, *27* (8), 85104.

(21) Wu, K.; Zhang, X.; Wang, J.; Li, X.; Chen, J. WS_2 as a Saturable Absorber for Ultrafast Photonic Applications of Mode-Locked and Q-Switched Lasers. *Opt. Express* **2015**, *23* (9), 11453.

(22) Lu, S. B.; Miao, L. L.; Guo, Z. N.; Qi, X.; Zhao, C. J.; Zhang, H.; Wen, S. C.; Tang, D. Y.; Fan, D. Y. Broadband Nonlinear Optical Response in Multi-Layer Black Phosphorus: An Emerging Infrared and Mid-Infrared Optical Material. *Opt. Express* **2015**, *23* (9), 11183.

(23) Zhang, H.; Lu, S. B.; Zheng, J.; Du, J.; Wen, S. C.; Tang, D. Y.; Loh, K. P. Molybdenum Disulfide (MoS_2) as a Broadband Saturable Absorber for Ultra-Fast Photonics. *Opt. Express* **2014**, *22* (6), 7249.

(24) Cai, W.; Shalaev, V. *Optical Metamaterials*; Springer: New York, 2010.

(25) Maier, S. A. *Plasmonics: Fundamentals and Applications*; Springer: Boston, MA, 2007.

(26) Aydin, K.; Ferry, V. E.; Briggs, R. M.; Atwater, H. A. Broadband Polarization-Independent Resonant Light Absorption Using Ultrathin Plasmonic Super Absorbers. *Nat. Commun.* **2011**, *2*, 517.

(27) Ding, F.; Jin, Y.; Li, B.; Cheng, H.; Mo, L.; He, S. Ultrabroadband Strong Light Absorption Based on Thin Multilayered Metamaterials. *Laser Photonics Rev.* **2014**, *8* (6), 946−953.

(28) Naguib, M. Chapter 4: Two-Dimensional Transition Metal Carbides and Carbonitrides. In *Nanomaterials Handbook*; Gogotsi, Y., Ed.; Taylor & Francis, CRC Press: Boca Raton, 2017; pp 83−102.

(29) Halim, J.; Kota, S.; Lukatskaya, M. R.; Naguib, M.; Zhao, M.-Q.; Moon, E. J.; Pitock, J.; Nanda, J.; May, S. J.; Gogotsi, Y.; Barsoum, M. W. Synthesis and Characterization of 2D Molybdenum Carbide (MXene). *Adv. Funct. Mater.* **2016**, *26* (18), 3118−3127.

(30) Anasori, B.; Lukatskaya, M. R.; Gogotsi, Y. 2D Metal Carbides and Nitrides (MXenes) for Energy Storage. *Nat. Rev. Mater.* **2017**, *2* (2), 16098.

(31) Naguib, M.; Gogotsi, Y. Synthesis of Two-Dimensional Materials by Selective Extraction. *Acc. Chem. Res.* **2015**, *48* (1), 128−135.

(32) Alhabeb, M.; Maleski, K.; Anasori, B.; Lelyukh, P.; Clark, L.; Sin, S.; Gogotsi, Y. Guidelines for Synthesis and Processing of Two-Dimensional Titanium Carbide ($Ti_3C_2T_x$ MXene). *Chem. Mater.* **2017**, *29* (18), 7633−7644.

(33) Halim, J.; Lukatskaya, M. R.; Cook, K. M.; Lu, J.; Smith, C. R.; Näslund, L.-Å.; May, S. J.; Hultman, L.; Gogotsi, Y.; Eklund, P.; Barsoum, M. W. Transparent Conductive Two-Dimensional Titanium Carbide Epitaxial Thin Films. *Chem. Mater.* **2014**, *26* (7), 2374−2381.

(34) Kajiyama, S.; Szabova, L.; Sodeyama, K.; Iinuma, H.; Morita, R.; Gotoh, K.; Tateyama, Y.; Okubo, M.; Yamada, A. Sodium-Ion Intercalation Mechanism in MXene Nanosheets. *ACS Nano* **2016**, *10* (3), 3334−3341.

(35) Lukatskaya, M. R.; Kota, S.; Lin, Z.; Zhao, M.-Q.; Shpigel, N.; Levi, M. D.; Halim, J.; Taberna, P.-L.; Barsoum, M. W.; Simon, P.; Gogotsi, Y. Ultra-High-Rate Pseudocapacitive Energy Storage in Two-Dimensional Transition Metal Carbides. *Nat. Energy* **2017**, *2* (8), 17105.

(36) Tian, Y.; Yang, C.; Que, W.; Liu, X.; Yin, X.; Kong, L. B. Flexible and Free-Standing 2D Titanium Carbide Film Decorated with Manganese Oxide Nanoparticles as a High Volumetric Capacity Electrode for Supercapacitor. *J. Power Sources* **2017**, *359*, 332−339.

(37) Yang, C.; Que, W.; Yin, X.; Tian, Y.; Yang, Y.; Que, M. Improved Capacitance of Nitrogen-Doped Delaminated Two-Dimensional Titanium Carbide by Urea-Assisted Synthesis. *Electrochim. Acta* **2017**, *225*, 416−424.

(38) Shahzad, F.; Alhabeb, M.; Hatter, C. B.; Anasori, B.; Man Hong, S.; Koo, C. M.; Gogotsi, Y. Electromagnetic Interference Shielding with 2D Transition Metal Carbides (MXenes). *Science* **2016**, *353* (6304), 1137−1140.

(39) Li, R.; Zhang, L.; Shi, L.; Wang, P. MXene Ti_3C_2: An Effective 2D Light-to-Heat Conversion Material. *ACS Nano* **2017**, *11* (4), 3752−3759.

(40) Jhon, Y. M. I.; Koo, J.; Anasori, B.; Seo, M.; Lee, J. H.; Gogotsi, Y.; Jhon, Y. M. I. Metallic MXene Saturable Absorber for Femtosecond Mode-Locked Lasers. *Adv. Mater.* **2017**, *29* (40), 1702496.

(41) Satheeshkumar, E.; Makaryan, T.; Melikyan, A.; Minassian, H.; Gogotsi, Y.; Yoshimura, M. One-Step Solution Processing of Ag, Au and Pd@MXene Hybrids for SERS. *Sci. Rep.* **2016**, *6* (1), 32049.

(42) Sarycheva, A.; Makaryan, T.; Maleski, K.; Satheeshkumar, E.; Melikyan, A.; Minassian, H.; Yoshimura, M.; Gogotsi, Y. Two-

DOI: 10.1021/acsphotonics.7b01439
ACS Photonics 2018, 5, 1115−1122

Dimensional Titanium Carbide (MXene) as Surface-Enhanced Raman Scattering Substrate. *J. Phys. Chem. C* **2017**, *121* (36), 19983−19988.
(43) Gramotnev, D. K.; Bozhevolnyi, S. I. Plasmonics beyond the Diffraction Limit. *Nat. Photonics* **2010**, *4* (2), 83−91.
(44) Mauchamp, V.; Bugnet, M.; Bellido, E. P.; Botton, G. a.; Moreau, P.; Magne, D.; Naguib, M.; Cabioc'h, T.; Barsoum, M. W. Enhanced and Tunable Surface Plasmons in Two-Dimensional Ti_3C_2 Stacks: Electronic Structure versus Boundary Effects. *Phys. Rev. B: Condens. Matter Mater. Phys.* **2014**, *89* (23), 235428.
(45) Jiang, X.; Liu, S.; Liang, W.; Luo, S.; He, Z.; Ge, Y.; Wang, H.; Cao, R.; Zhang, F.; Wen, Q.; Li, J.; Bao, Q.; Fan, D.; Zhang, H.; Jiang, X.; Liang, W.; Luo, S.; He, Z.; Ge, Y.; Wang, H.; Zhang, F.; Fan, D.; Zhang, H. Broadband Nonlinear Photonics in Few-Layer MXene $Ti_3C_2T_x$ (T = F, O, or OH). *Laser Photonics Rev.* **2017**, 1700229.
(46) Kildishev, A. V.; Boltasseva, A.; Shalaev, V. M. Planar Photonics with Metasurfaces. *Science* **2013**, *339* (6125), 1232009−1232009.
(47) Lipatov, A.; Alhabeb, M.; Lukatskaya, M. R.; Boson, A.; Gogotsi, Y.; Sinitskii, A. Effect of Synthesis on Quality, Electronic Properties and Environmental Stability of Individual Monolayer Ti_3C_2 MXene Flakes. *Adv. Electron. Mater.* **2016**, *2* (12), 1600255.
(48) Hong Ng, V. M.; Huang, H.; Zhou, K.; Lee, P. S.; Que, W.; Xu, J. Z.; Kong, L. B. Recent Progress in Layered Transition Metal Carbides And/or Nitrides (MXenes) and Their Composites: Synthesis and Applications. *J. Mater. Chem. A* **2017**, *5* (7), 3039−3068.
(49) Hantanasirisakul, K.; Zhao, M.-Q.; Urbankowski, P.; Halim, J.; Anasori, B.; Kota, S.; Ren, C. E.; Barsoum, M. W.; Gogotsi, Y. Fabrication of $Ti_3C_2T_x$ MXene Transparent Thin Films with Tunable Optoelectronic Properties. *Adv. Electron. Mater.* **2016**, *2* (6), 1600050.
(50) Hope, M. A.; Forse, A. C.; Griffith, K. J.; Lukatskaya, M. R.; Ghidiu, M.; Gogotsi, Y.; Grey, C. P. NMR Reveals the Surface Functionalisation of Ti_3C_2 MXene. *Phys. Chem. Chem. Phys.* **2016**, *18* (7), 5099−5102.
(51) Wang, H.-W.; Naguib, M.; Page, K.; Wesolowski, D. J.; Gogotsi, Y. Resolving the Structure of $Ti_3C_2T_x$ MXenes through Multilevel Structural Modeling of the Atomic Pair Distribution Function. *Chem. Mater.* **2016**, *28* (1), 349−359.
(52) Han, M.; Yin, X.; Wu, H.; Hou, Z.; Song, C.; Li, X.; Zhang, L.; Cheng, L. Ti_3C_2 MXenes with Modified Surface for High-Performance Electromagnetic Absorption and Shielding in the X-Band. *ACS Appl. Mater. Interfaces* **2016**, *8* (32), 21011−21019.
(53) Liu, J.; Zhang, H.-B.; Sun, R.; Liu, Y.; Liu, Z.; Zhou, A.; Yu, Z.-Z. Hydrophobic, Flexible, and Lightweight MXene Foams for High-Performance Electromagnetic-Interference Shielding. *Adv. Mater.* **2017**, *29* (38), 1702367.
(54) Ren, C. E.; Hatzell, K. B.; Alhabeb, M.; Ling, Z.; Mahmoud, K. A.; Gogotsi, Y. Charge- and Size-Selective Ion Sieving Through $Ti_3C_2T_x$ MXene Membranes. *J. Phys. Chem. Lett.* **2015**, *6* (20), 4026−4031.
(55) Romer, F. M.; Wiedwald, U.; Strusch, T.; Halim, J.; Mayerberger, E.; Barsoum, M. W.; Farle, M. Controlling the Conductivity of Ti_3C_2 MXenes by Inductively Coupled Oxygen and Hydrogen Plasma Treatment and Humidity. *RSC Adv.* **2017**, *7* (22), 13097−13103.
(56) Dillon, A. D.; Ghidiu, M. J.; Krick, A. L.; Griggs, J.; May, S. J.; Gogotsi, Y.; Barsoum, M. W.; Fafarman, A. T. Highly Conductive Optical Quality Solution-Processed Films of 2D Titanium Carbide. *Adv. Funct. Mater.* **2016**, *26* (23), 4162−4168.
(57) Miranda, A.; Halim, J.; Barsoum, M. W.; Lorke, A. Electronic Properties of Freestanding $Ti_3C_2T_x$ MXene Monolayers. *Appl. Phys. Lett.* **2016**, *108* (3), 33102.
(58) Lashgari, H.; Abolhassani, M. R.; Boochani, A.; Elahi, S. M.; Khodadadi, J. Electronic and Optical Properties of 2D Graphene-like Compounds Titanium Carbides and Nitrides: DFT Calculations. *Solid State Commun.* **2014**, *195*, 61−69.
(59) Pors, A.; Albrektsen, O.; Radko, I. P.; Bozhevolnyi, S. I. Gap Plasmon-Based Metasurfaces for Total Control of Reflected Light. *Sci. Rep.* **2013**, *3*, 2155.
(60) Jung, J.; Søndergaard, T.; Bozhevolnyi, S. I. Gap Plasmon-Polariton Nanoresonators: Scattering Enhancement and Launching of Surface Plasmon Polaritons. *Phys. Rev. B: Condens. Matter Mater. Phys.* **2009**, *79* (3), 35401.
(61) Bozhevolnyi, S. I.; Søndergaard, T. General Properties of Slow-Plasmon Resonant Nanostructures: Nano-Antennas and Resonators. *Opt. Express* **2007**, *15* (17), 10869−10877.
(62) Oulton, R. F.; Sorger, V. J.; Genov, D. A.; Pile, D. F. P.; Zhang, X. A Hybrid Plasmonic Waveguide for Subwavelength Confinement and Long-Range Propagation. *Nat. Photonics***2008**249650010.1038/nphoton.2008.131
(63) Anker, J. N.; Hall, W. P.; Lyandres, O.; Shah, N. C.; Zhao, J.; Van Duyne, R. P. Biosensing with Plasmonic Nanosensors. *Nat. Mater.* **2008**, *7* (6), 442−453.
(64) Joy, N. A.; Nandasiri, M. I.; Rogers, P. H.; Jiang, W.; Varga, T.; Kuchibhatla, S. V. N. T.; Thevuthasan, S.; Carpenter, M. A. Selective Plasmonic Gas Sensing: H_2, NO_2, and CO Spectral Discrimination by a Single Au-CeO_2 Nanocomposite Film. *Anal. Chem.* **2012**, *84* (11), 5025−5034.

DOI: 10.1021/acsphotonics.7b01439
ACS Photonics 2018, 5, 1115−1122